Multi-Scale Ground Deformation in Beijing Plain Revealed by a Joint 2D-FFT and MGWR Decomposition of InSAR Observation

Nian Feng, Lei Xie, Wenbin Xu, and Miao Yu

***Abstract*—Understanding urban surface deformation from InSAR one dimensional line-of-sight observation is challenging due to the interplay of various natural and anthropogenic driving factors. This article proposes a novel multiscale InSAR deformation decomposition method that integrates two-dimensional fast Fourier transform with a multiscale geographically weighted regression model. We apply this method to analyze urban ground deformation in the Beijing Plain, China, using Sentinel-1 data from 2016 to 2023. The results identify five significant subsidence areas with the maximum subsidence reaching −360 mm. The decomposed large-scale component (4–8 km) correlates closely with the thickness of Quaternary sediments and variations of groundwater. The medium-scale component (1–3 km) is associated with the urban construction activities, while the small-scale deformation (<0.6 km) reveals localized subsidence along subway with tunnel construction. These findings demonstrate the effectiveness of the proposed method in capturing the multiscale deformation patterns, especially the concealed small-scale deformation, through a single orbit of InSAR observation. Therefore, it shows high potentials to improve the urban infrastructure safety such as subway engineering.**

***Index Terms*—Interferometric synthetic aperture radar (InSAR), multiscale, subway, urban deformation decomposition.**

I. Introduction

INTERFEROMETRIC synthetic aperture radar (InSAR), with its advantages of wide coverage and high measurement accuracy, has been widely applied in different fields, including landslides [1], [2], volcanoes [3], earthquakes [4], and ground subsidence [5], [6], [7], [8], [9], [10]. In metropolitan areas, InSAR has shown significant potential in monitoring urban subsidence, as demonstrated in Mexico City [11], Beijing [12], [13], Shanghai [14], and Bangkok [15]. These InSAR-based measurements reveal the evolution and extension of urban subsidence, offering valuable insights for disaster mitigation.

The Beijing Plain, covering an area of about 6200 km^2, is located in the southeastern part of the Beijing city (see Fig. 1) [12]. Geologically, the Beijing Plain is affected by multiple active faults, exhibiting significant tectonic control characteristics. The region also hosts extensive Quaternary deposits, with thicknesses increasing from northwest to southeast, reaching several hundred meters. These factors increase the susceptibility to regional ground subsidence [16]. In terms of human interventions, Beijing's urbanization process has led to over-exploitation of groundwater since 1960s. Under the combined influence of natural and human factors, multiple subsidence funnels with varying extents and deformation degrees have formed in the Beijing Plain [17]. This poses a threat to urban infrastructure safety and underscores the urgent need for effective monitoring and integrated prevention strategies.

Most existing studies focus on large-scale subsidence with a spatial scale of tens of kilometers. However, urban subsidence is a combination of different scales of deformations. The prominent large-scale deformation may mask the medium and small scales deformation, challenging the analysis of deformation on scales ranging from a few hundred meters to several kilometers.

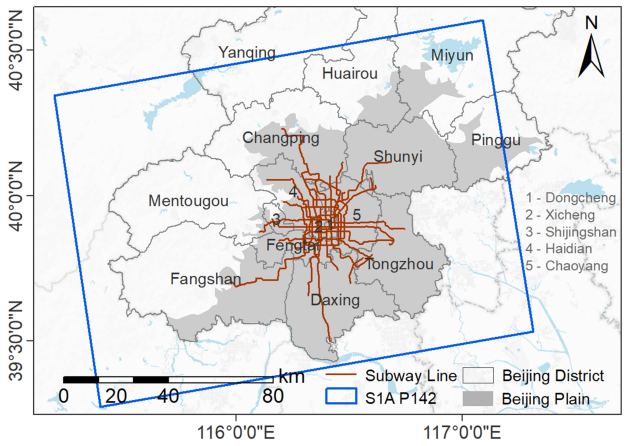

Fig. 1. Location of Beijing city and Beijing plain. Brown lines represent subway routes. The blue rectangle is the footprint of Sentinel-1 images used in this article.

Received 22 January 2025; revised 4 April 2025; accepted 22 May 2025. Date of publication 26 May 2025; date of current version 13 June 2025. This work was supported in part by the Natural Science Foundation of Hunan Province under Grant 2024JJ3031 and Grant 2025JJ60239, in part by Hunan Provincial Transportation Science and Technology Progress and Innovation Plan Project under Grant 202211, in part by the National Natural Science Foundation of China under Grant 42174023 and Grant 42304037, in part by the National Key Research and Development Program under Grant 2022YFB3903602, in part by the Frontier Cross Research Project of Central South University under Grant 2023QYJC006, in part by the Science and Technology Innovation Program of Fujian Province under Grant 2021Y3001, and in part by the Science and Technology Innovation Program of Hunan Province under Grant 2023SK2012. *(Corresponding author: Lei Xie.)*

Nian Feng, Lei Xie, and Wenbin Xu are with the School of Geosciences and Info-Physics, Central South University, Changsha 410083, China (e-mail: feynman31@qq.com; leixie_geo@csu.edu.cn; wenbin.xu@csu.edu.cn).

Miao Yu is with the Beijing Urban Construction Survey, Design and Research Institute Company Ltd., Beijing 100101, China (e-mail: yumiao4503210@126.com).

Digital Object Identifier 10.1109/JSTARS.2025.3573810

For example, Chen et al. [18] used entropy analysis to study the surface subsidence during subway construction and operation. They found that subsidence around subway stations exhibited typical regional subsidence patterns. Duan et al. [19] proposed an improved MMTI-TSF method to monitor long-term deformation of the Beijing subway network. Their research found a close relationship between subsidence along subway lines and the subsidence centers. These studies indicate that the large-scale deformation affect the interpretation of medium and small-scale deformations, leading to an incomplete understanding of localized deformation.

Despite directly interpretation of the InSAR deformation to the localized deformation, different InSAR decomposition method proposed. For example, Lai et al. [20] used independent component analysis in Beijing to distinguish deformation characteristics from strata information. They found linear subsidence and uplift, decelerating subsidence, and periodic deformation. Xu et al. [21] employed principal component analysis to extract three principal components of temporal deformation, which were related to groundwater changes, quaternary sediment thickness (QST), and rainfall related periodic deformation. However, these methods primarily extract different subsidence patterns from InSAR data in temporal domain. They have not effectively separated deformation components at multiple spatial scales. This limits the spatial interpretation of multiscale deformation features and the analysis of their driving mechanisms. Solano-Rojas et al. [22] proposed the two-dimensional fast Fourier transform (2D-FFT) band-pass filtering method to decompose the deformation field into multiple scales. Each component is associated with distinct influencing factors, such as geological conditions, civil construction activities, metro-related subsidence, etc. They validated this method in metro system of Mexico City, and demonstrated that the mid-wavelength component effectively reveals hidden differential vertical displacement signals [23]. Subsequently, this method has been successfully applied to Shanghai [24] and the Guangdong-Hong Kong-Macao Greater Bay Area [25] to analyze the spatial characteristics of multiscale deformation patterns and identify local subsidence samples. While these studies demonstrate the effectiveness of 2D-FFT in separating deformation in the complex urban environment, they do not offer a comprehensive quantitative assessment of the driving mechanisms behind the isolated deformation component. To bridge this gap, our study integrates the 2D-FFT method with multiscale geographically weighted regression model (MGWR), enabling scale-specific regression analysis and yielding a more nuanced interpretation of urban subsidence mechanisms.

In this article, we propose a new multiscale InSAR decomposition and analysis method for the urban deformation scenario. It integrates 2D-FFT and a MGWR model to decompose the deformation in the frequency domain.

The rest of this article is organized as follows. In Section II, we introduce the dataset including the InSAR and other auxiliary data used in this article. Section III describes the proposed method focusing on integration of the 2D-FFT and MGWR. In Section IV, we present the results of deformation separation at various scales and the regression coefficients for the influencing factors. Section V discusses the main driving factors and subsidence mechanisms related to deformation components across different scales. Finally, Section VI concludes this article.

II. Dataset and Data Process

A. SAR Data

This article used 76 scenes of C-band Sentinel-1 data without radar radio frequency interference from August 2016 to December 2023. The satellite track is 142, with a spatial resolution of 5 m $\times$ 20 m (range $\times$ azimuth) in single-look complex format. We used small baseline subset InSAR (SBAS-InSAR) method to extract the subsidence of Beijing Plain. SBAS-InSAR technique is an effective method for estimating surface deformation through time-series SAR imagery. Its primary objective is to integrate multiple SAR images and select appropriate subsets of baselines. This helps to mitigate temporal and spatial decorrelation and meets the demands of urban monitoring [26]. To effectively capture long-term, slow surface deformation, a temporal baseline threshold of 290 days and a perpendicular baseline of 150 m were set. Differential interferometric processing was carried out using GAMMA software [27]. We used a 30 m SRTM DEM to simulate the topographic phase, which allowed for the removal of the surface elevation phase from the interferogram. Adaptive filtering was then applied to improve the quality of the interferogram. Phase unwrapping was performed using the minimum cost flow method, with a reference to the stable Forbidden City area. We applied temporal filtering with a 60-day temporal window to mitigate the tropospheric effects. Finally, singular value decomposition was applied to solve the time-series deformation. As surface deformation in the Beijing Plain is primarily dominated in the vertical direction [12], the solved LOS deformation is converted to the vertical direction using the local incidence angle from radar geometry.

B. Potential Influencing Factors Data

Urban ground subsidence is influenced by various factors, including geological and topographic conditions, hydrologic factors, human activities, and natural environmental factors. To better quantify the contributions from different sources, we collected eight factors related to ground subsidence in the Beijing Plain.

1) The geological and topographic factors include the digital elevation model (DEM), slope, QST, and the distance to faults (DFault). We used STRM DEM for topography and slope estimation. The QST map and fault distribution data were from field investigations.
2) Hydrologic factors include changes in groundwater level (GWL) and distance from water systems (DWater). GWL data were obtained from groundwater wells during May–November, 2023. Water system data were from open street map.
3) Human activities and natural environmental factors include NDVI and population density (POP). The NDVI data were obtained from the MOD13A3 dataset released by NASA. Population density was obtained from Chen et al. [28].

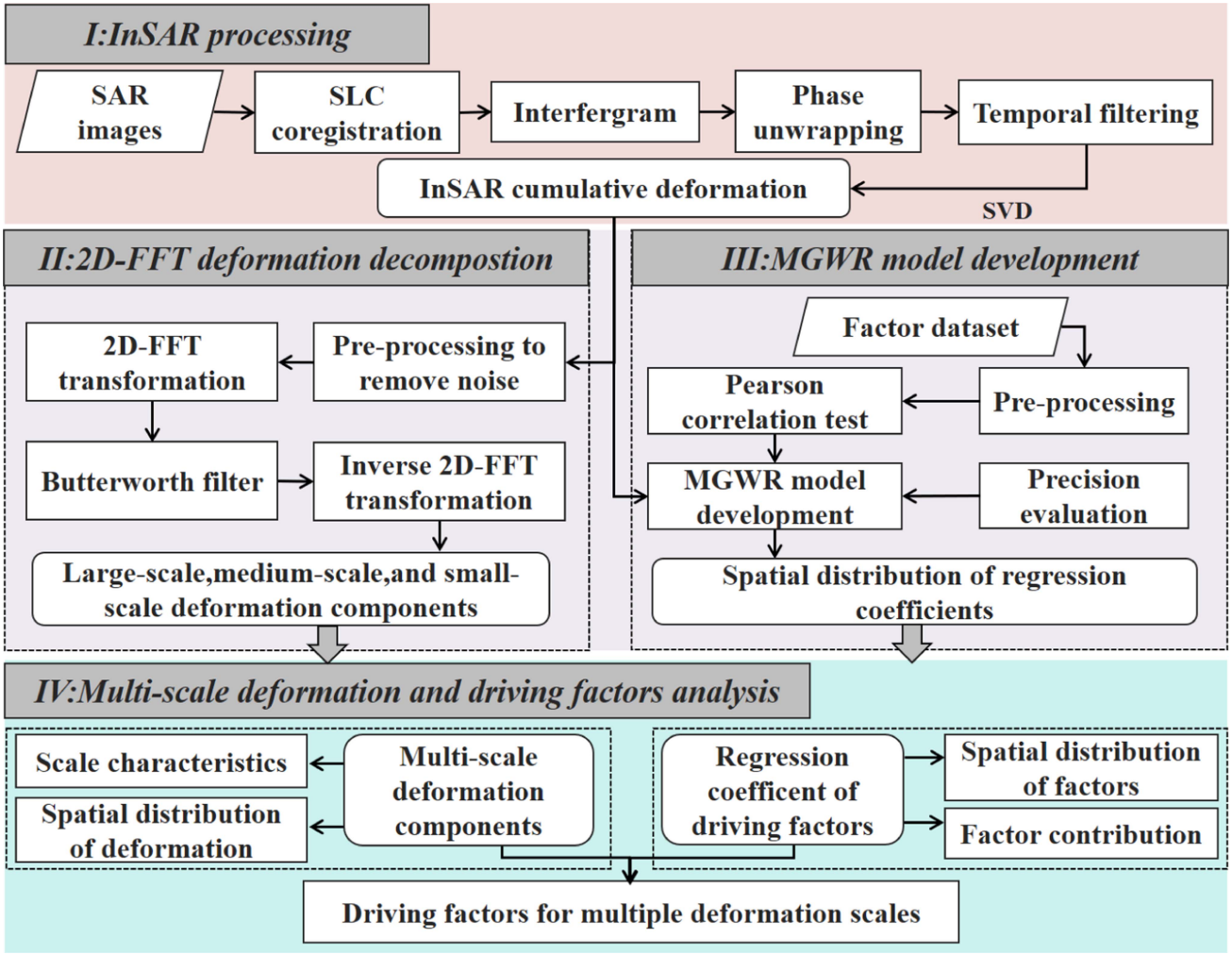

Fig. 2. Flowchart of the study. (1) InSAR data processing. (2) and (3) Proposed integrated 2D-FFT decomposition and MGWR modeling method. (4) Driving factors analysis.

III. Integrated 2D-FFT and MGWR Method for Multiscale InSAR Deformation Decomposition and Analysis

To better interpret the driving mechanisms of deformation at different scales, this article proposes an integrated 2D-FFT and MGWR method for InSAR deformation decomposition (see Fig. 2). The first step is following the conventional SBAS-InSAR method to extract the surface deformation. The second part is separating deformation signals at different scales using the 2D-FFT method. Third, a MGWR model is determined to assess the contribution of potential factors to the surface deformation. Finally, the driving mechanisms of deformation at different scales are analyzed.

A. 2D-FFT Decomposition for InSAR Deformation

Deformation at different scales shows various spatial distribution characteristics. Traditional deformation separation methods, such as statistical analysis and wavelet decomposition [29], demonstrate effectiveness in identifying deformation patterns with predominant driving source and capturing temporal deformation trends in time domain. However, in the Beijing Plain, subsidence manifests across heterogeneous spatial scales, leading to the superposition of regional and local deformation. Therefore, using the threshold-based method to identify regional-scale and finer subsidence, may omit or even overlook local deformation features [22], [25]. Instead, spatial frequency-based analysis provides a new perspective for multiscale deformation separation. The low-frequency threshold can be determined by the inflection point from the mean power spectrum using the sliding window and bottom-up (SWAB) method [30]. The threshold of high-frequency is determined by the deformation characteristics of the study area. Correspondingly, the medium threshold is the interval between low- and high-frequency thresholds. The transfer function of the Butterworth filter is then applied to these wavelength bands [31]

$$H(u,v)_1 = 1/\left(1+\left[D(u,v)/D_0\right]^{2n}\right) \tag{1}$$

$$H(u,v)_2 = 1/\left(1+\left[D_1/D(u,v)\right]^{2n}\right) \tag{2}$$

$$H(u,v)_3 = 1 - 1/\left(1 + \left[D * W/\left(D^2 - D_2^2\right)\right]^{2n}\right) \quad (3)$$

where $H(u,v)_{1,2,3}$ represent the filtering functions, $D(u,v)$ denotes the distance from the frequency center. D_0, D_1, D_0 correspond to the cutoff frequencies for low, high, and medium frequencies, respectively. W represents the bandwidth, and n is the order of Butterworth filter (i.e., $n = 2$). Finally, the inverse Fourier transform is applied to recover the deformation in different scales.

B. Multiscale Geographically Weighted Regression (MGWR) Model

The geographically weighted regression model can explore spatial heterogeneity by determining the optimal bandwidth [32]. However, it analyzes all influencing factors on the same spatial scale, which may simplify complex geographic phenomena. To address this limitation, the MGWR model was developed by incorporating multiscale effects using variable bandwidths, thereby effectively handling geographic multiscaling [33], as follows:

$$y_i = \beta_{bw0}(u_i, v_i) + \sum_{k=1}^{m} \beta_{bwk}(u_i, v_i)\, x_{ik} + \varepsilon_i \quad (4)$$

in which y_i is the dependent variable at the ith location, x_{ik} represents the kth independent variable at the ith location, $\beta_{bw0}(u_i, v_i)$ is the intercept parameter, $\beta_{bwk}(u_i, v_i)$ is the local coefficient estimate, and ε_i is the residual term.

Next, the input deformation and other potential influencing factors are resampled to a uniform grid and standardized to eliminate dimensional effects between independent variables. The Pearson correlation coefficient (R^2) is used to examine the collinearity between different variables. Variables exhibiting high collinearity (i.e., $|R^2| \to 1$) are removed to enhance model reliability. The fitness can be evaluated using indicators such as the adjusted R-squared (Adj.R^2), residual sum of squares (RSS), and the improved akaike information criterion (AICc). A better model fit corresponds to a larger R^2, the smaller RSS and AICc. These indicators are defined as follows:

$$\text{Adj.}R^2 = 1 - \frac{\sum_{i=1}^{m}(\widehat{y_i} - y_i)^2}{\sum_{i=1}^{m}\left(\overline{y} - y_i\right)^2} \cdot \frac{m-1}{m-k-1} \quad (5)$$

$$\text{RSS} = \sum_{i=1}^{m}\left(\widehat{y_i} - y_i\right)^2 \quad (6)$$

$$\text{AIC}c = -2 \cdot ln\left(L\right) + 2k + \frac{2k(k+1)}{m-k-1} \quad (7)$$

where m is the sample size, y_i and $\widehat{y_i}$ represent the true value and predicted value of the ith element, respectively. $\ln(L)$ is the log−likelihood value of the model′s maximum likelihood estimate, and k is the number of parameters in the model.

IV. Results

A. InSAR Deformation and Validation

We used the SBAS-InSAR technique to obtain the cumulative deformation in the Beijing Plain from August 2016 to December 2023. The LOS deformation is then converted into vertical displacement by pixel-wise local incidence angles [see Fig. 3(a)]. The Beijing Plain experiences widespread ground subsidence with distinct regional characteristics. Approximately 16.6% of the area has cumulative subsidence exceeding −50 mm. This subsidence is concentrated in five major subsidence funnels: the Haidian-Changping subsidence funnel (S1), the Daxing subsidence funnel (S2), the Chaoyang-Tongzhou subsidence funnel (S3), and two subsidence funnels in Shunyi (S4 and S5). The total area of these subsidence funnels is approximately 1562 km^2, accounting for 24.4% of the Beijing Plain. Among these, the Chaoyang–Tongzhou subsidence funnel (S3) experiences the most severe subsidence, with an average cumulative subsidence of −115 mm and the maximum cumulative subsidence reaching −360 mm. The InSAR measurement agrees well with the leveling measurement [see Fig. 3(c)], with a correlation of 0.94, and a root mean square error of ∼10 mm. This demonstrates the reliability of the extracted InSAR deformation.

Taking a 400 m buffer zone around the subway network, 73% of the subway network exhibits cumulative deformation less than 20 mm. However, the deformation of the subway lines passing through the subsidence funnel area is significantly increased. The east-west oriented subway lines 6, 7, and 17, the north-south oriented lines 27 and 5, as well as the ring-shaped lines 2 and 10 (see Fig. 4) show that, while overall deformation is relatively smooth, certain sections experience significant uneven deformation.

Specifically, for subway lines 6, 7, and 17 that pass through the center or edges of the S3 funnel, the average cumulative deformations are −38, −55, and −20 mm, respectively, and the maximum deformations reach −184, −265, and −242 mm, respectively. For line 27, which passes through the S1 subsidence funnel, the average cumulative through the S2 subsidence funnel is only −1 mm, but the maximum cumulative deformation is −115 mm. In contrast, the deformation along line 2 and line 5 remains stable, as these lines do not pass through subsidence funnels.

In contrast, deformation along lines 2 and 5 remains stable, as these lines do not intersect with subsidence funnels and exhibit deformation consistent with the subway's operational stage. It is noteworthy that the cumulative deformation average of the circular line 10 is 4 mm, with the maximum cumulative deformation reaching −100 mm. This indicates that most of the deformation along this line is uplift, while deformation gradients intensify near the edges of the subsidence funnels.

These results suggest that the overlapping deformation mechanisms makes it difficult to distinguish the local deformation signals. Therefore, in areas with complex driving mechanisms, separating deformation signal is essential for promptly identify local deformation and driving mechanism.

B. Multiscale Deformation Components

The low-frequency threshold was determined through identification of the spectral inflection point at 0.0918 on the raw power spectrum using SWAB analysis, corresponding to a spatial wavelength of 3267 m [see Fig. 5(b)]. Given the negligible impact of fine-scale variations to large-scale deformation, a conservative low-frequency threshold of 3000 m was established. Cross-sectional analysis along three profiles between Yong'anli

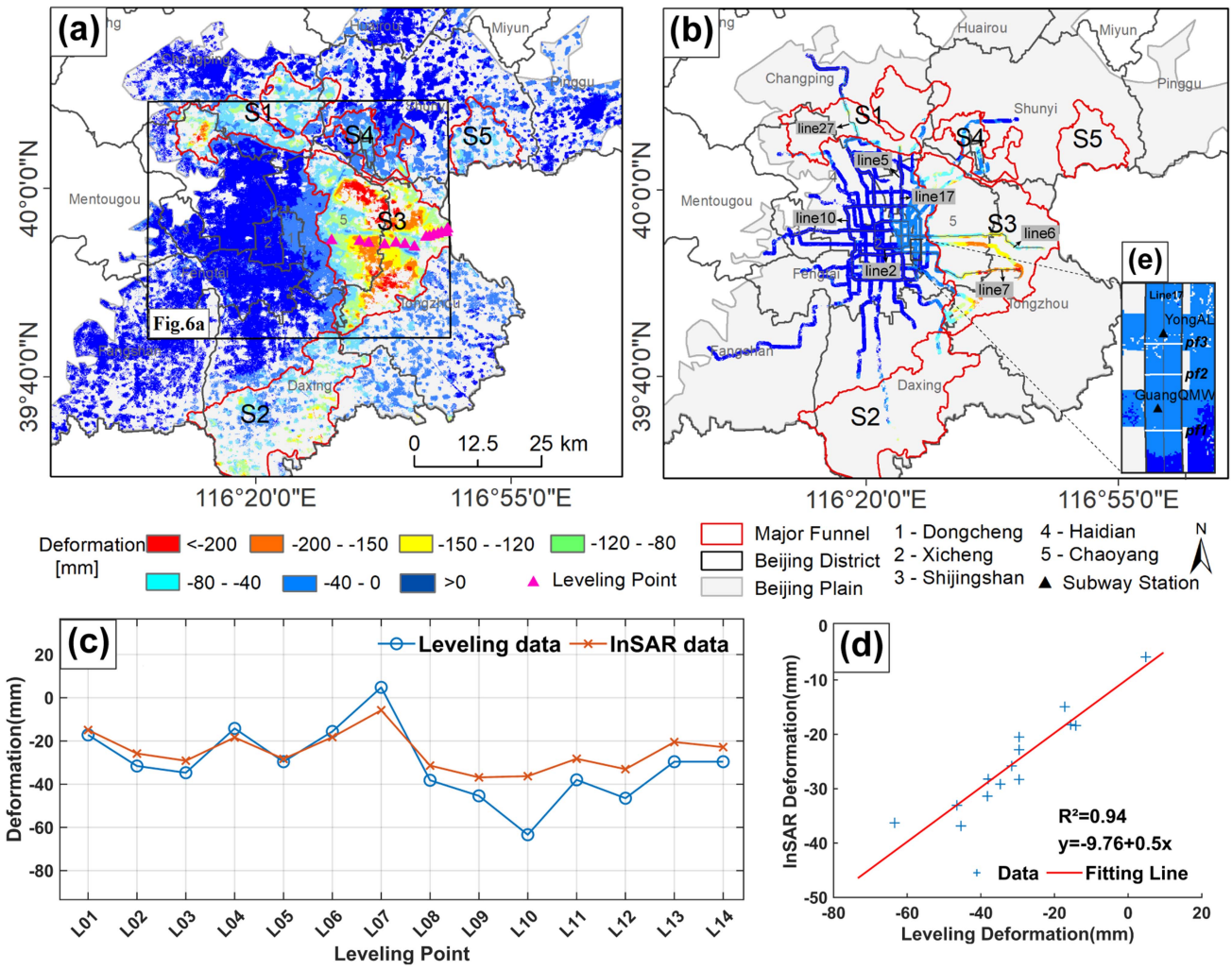

Fig. 3. Result of InSAR deformation and validation. (a) Cumulative vertical deformation of Beijing plain area from 2016 to 2023. (b) Vertical deformation of the subway network. (c) and (d) Comparison between InSAR and leveling data during the period from April 2019 to September 2019. The locations of leveling points are marked as magenta triangles in Fig. 3(a). (e) Profiles of subway line 17 for high-frequency threshold determination.

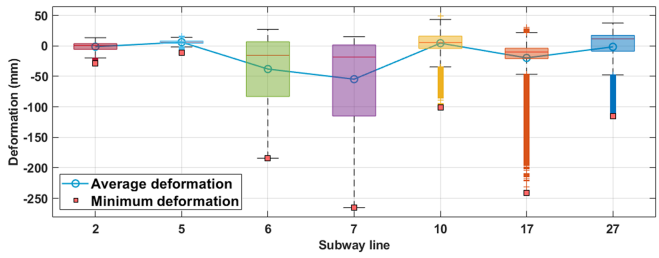

Fig. 4. Statistics of cumulative deformation along the subway line.

and Panjiayuan West stations on Beijing Metro Line 17 revealed subway-induced deformation within a 300–520 m radius. This finding aligns with previous metro impact studies in Beijing [34], Chengdu [35], and Guangdong [36], which consistently reported 400–600 m influence zones. Accounting for Sentinel-1's 5 × 20 m spatial resolution constraints, the high-frequency threshold was defined at 600 m to ensure detectable deformation patterns. Based on these thresholds, we performed deformation decomposition using the 2D-FFT method, resulting in large, medium, and small-scale deformation components. It can be observed that in areas with more severe subsidence, different subsidence modes coexist (see Fig. 6).

The large-scale deformation component is spatially smooth and similar to the original InSAR deformation results [see Fig. 6(b)]. It mainly covers the major funnels with 4–8 km along the profile [see Fig. 6(f)]. The magnitude of large-scale deformation component is comparable to the original deformation field. This indicates that the large-scale component primarily reflects the overall trend of regional deformation and is the main contributor to the original deformation. In contrast, the medium-scale deformation component shows a significant reduction in both deformation scale and magnitude. It is concentrated within a 1–3 km range [see Fig. 6(g)] and exhibits a clustered spatial distribution [see Fig. 6(c)]. The medium-scale deformation are located at the center and edges of the subsidence funnels. However, no significant deformation signal is observed in the city center, revealing the joint influence of local activities and geological structural differences on deformation. The small-scale deformation component has the smallest scale and deformation

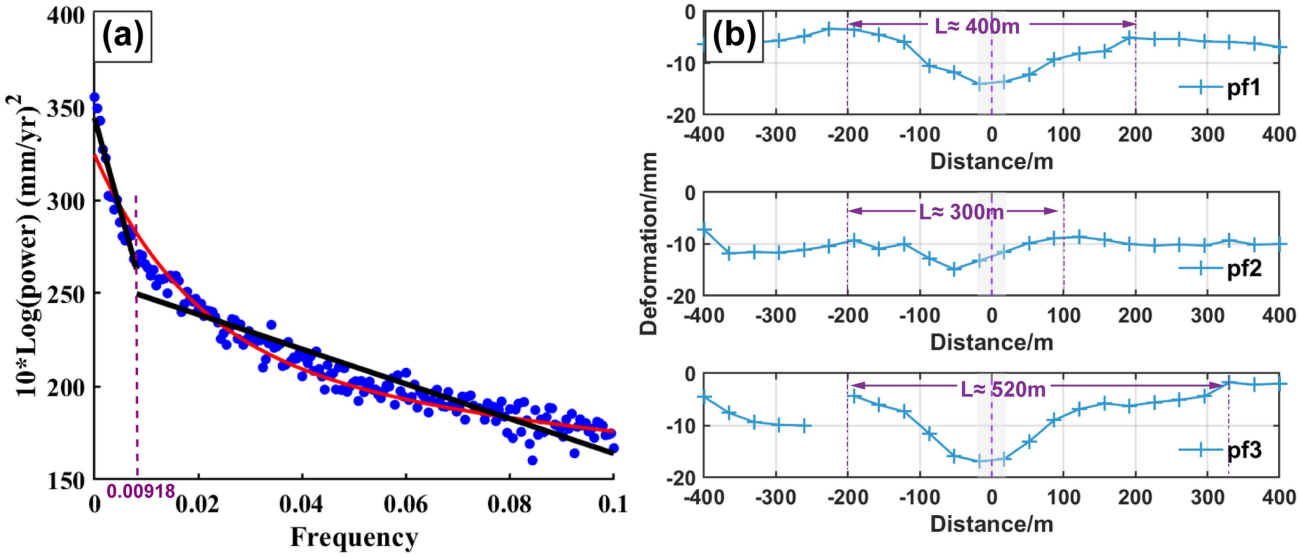

Fig. 5. Threshold selection for band-pass filtering. (a) Threshold of low-frequency: the average power spectrum. The two black lines represent the breakpoints detected by the SWAB, and the red line is the best-fit linear curve used to determine the cutoff frequency. (b) Threshold of high-frequency: Deformation of profiles along subway line 17 [the locations of pf1, pf2, and pf3 are marked in Fig. 3(e)].

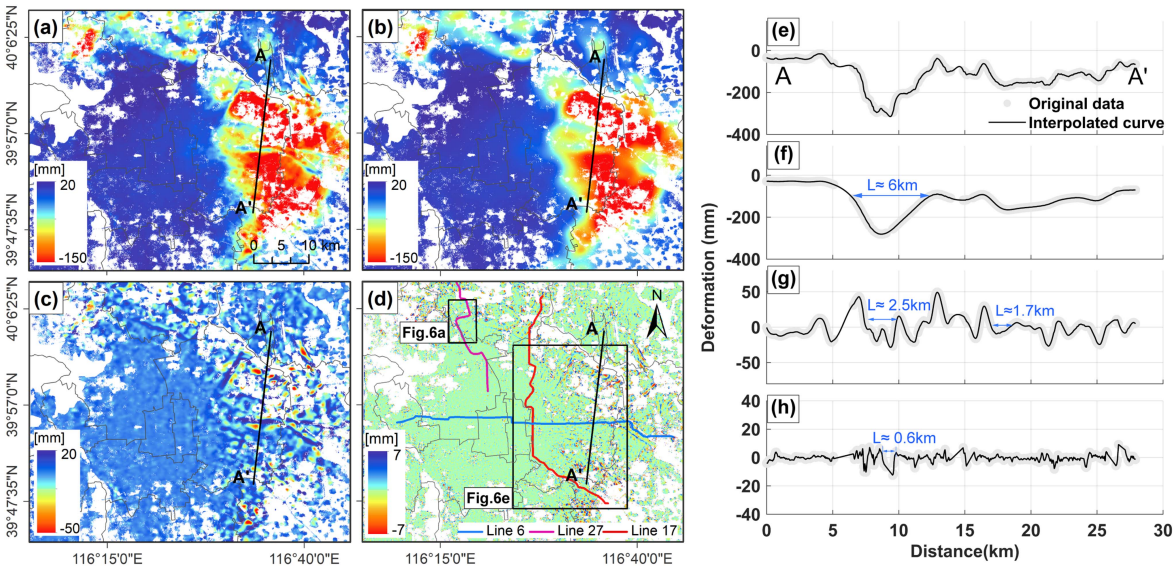

Fig. 6. Decomposed deformation components in Beijing Plain. (a) Original deformation. (b) Large-scale deformation component. (c) Medium-scale deformation component. (d) Small-scale deformation component. (e-h) Deformation along profile A-A' for original deformation, large-scale component, medium-scale component, and small-scale component, respectively.

magnitude [see Fig. 6(h)], with no obvious regularity in its spatial distribution [see Fig. 6(d)].

Overall, the contribution of large-scale, medium-scale, and small-scale deformation components to the original deformation decreases sequentially, but the level of detailed features gradually increases. Therefore, the small-scale deformation component is easily masked by the large- and medium- components (see Fig. 7).

C. Contribution of Driving Factor

The MGWR model reconstructs the deformation and quantifies the degree of contributions for different influencing factors. The Pearson correlation coefficient of the MGWR model is calculated to analyze the relationship between the independent variables. The result showed a correlation of 0.74 between DEM data and the QST data, leading to the exclusion of DEM for independence in analysis [see Fig. 8(d)].

The histogram of prediction errors for spatial points within the study area indicates that the absolute error for most spatial points is within 20 mm [see Fig. 8(c)]. Additionally, the model's fitting accuracy metrics were calculated as Adj.$R^2 = 0.989$, AICc= -12518, and RSS $= 130.65$, indicating that the model fitting is well-suited.

To quantify the influence of different variables at various spatial locations, the model calculated the mean, minimum,

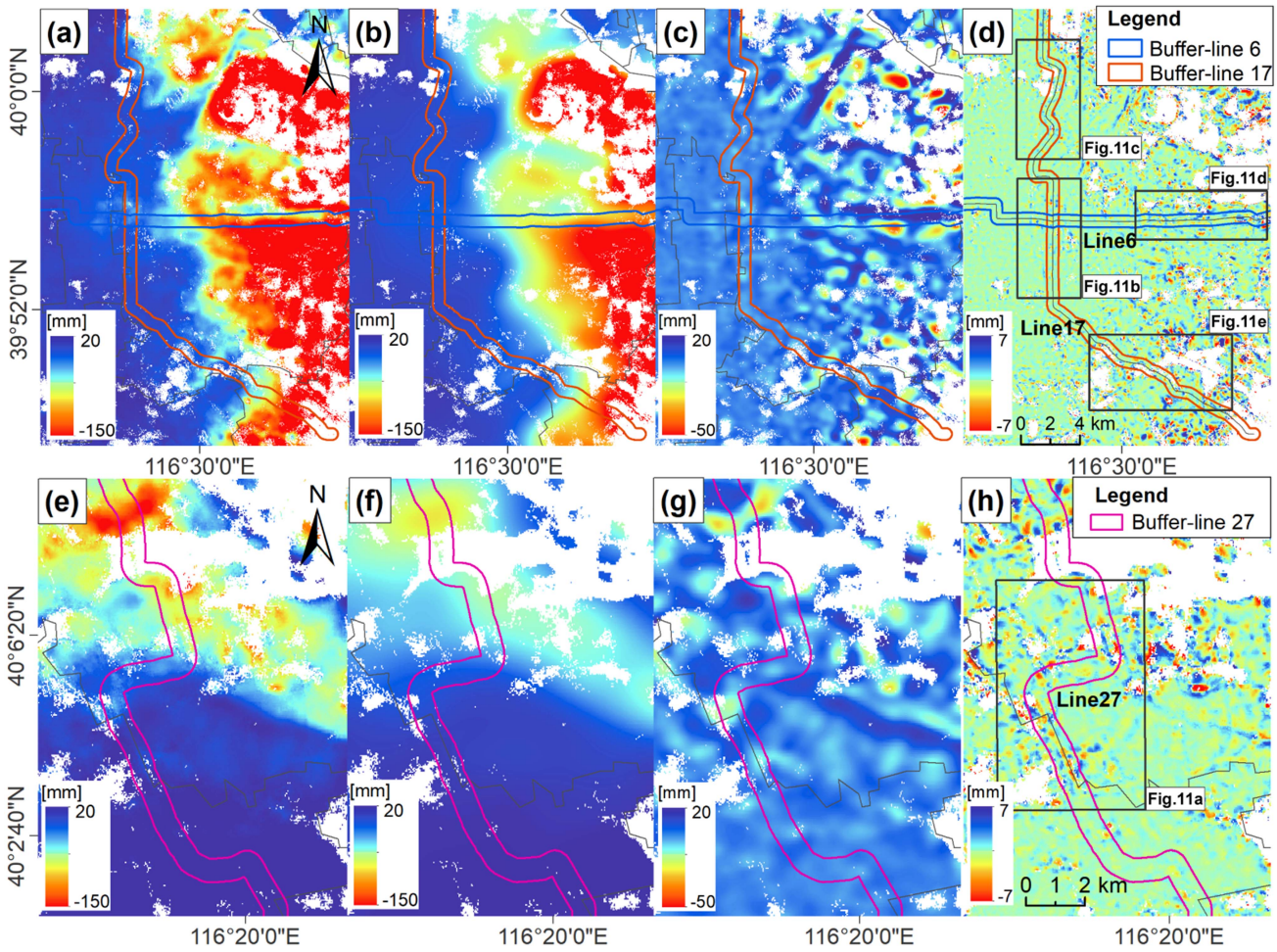

Fig. 7. Multiscale deformation components along the subway. (a) and (e) Original deformation. (b) and (f) Large-scale deformation components. (c) and (g) Medium-scale deformation components. (d) and (h) Small-scale deformation components.

TABLE I
MGWR MODEL COEFFICIENT FOR INFLUENCING FACTORS

Variable	Mean	Std	Min	Median	Max
SLOPE	0.003	0.034	-0.284	0.001	0.285
POP	-0.005	0.083	-0.719	0.002	0.529
GWL	-0.119	0.719	-2.89	-0.046	3.764
QST	-0.266	0.725	-4.522	-0.133	2.448
DFAULT	-0.011	0.203	-1.203	-0.003	0.812
DWATR	-0.01	0.139	-1.443	0.001	0.767
NDVI	0.008	0.044	-0.313	0.005	0.342

maximum, median, and standard deviation of the weight coefficients for seven variables (see Table I). The results indicate that QST and GWL changes are the primary driving factors of surface deformation, with mean regression coefficients of -0.266 and -0.119, respectively. This indicates that the negative effect on deformation is dominant. These DFault and DWater follow, with close but relatively small effects on deformation. In contrast, slope, population density, and NDVI show no significant effects on deformation in the study area, with mean regression coefficients less than 0.01.

V. DISCUSSION

A. *Large-Scale Deformation*

Large-scale deformation is typically closely related to factors such as geological environment and extensive changes in GWL [22]. In the Beijing Plain, large-scale regional subsidence is primarily caused by GWL changes, controlled by compressible layer thickness, faults, and other structural factors [37].

Large-scale deformation is predominantly distributed in the subsidence funnel S1, S4, and S3 regions, aligning well with the contour lines of QST [see Fig. 9(a)]. Moreover, it closely correlates spatially with its coefficients. This reflects that the dominant influence of geological conditions on regional ground deformation [38], [39], as thickness of compressible layers within the Quaternary sediments provide foundation of ground deformation. Specifically, in regions with relatively thin (<110 m) or thick (>150 m) compressible layers, deformation exhibits a linear or power-law correlation, predominantly

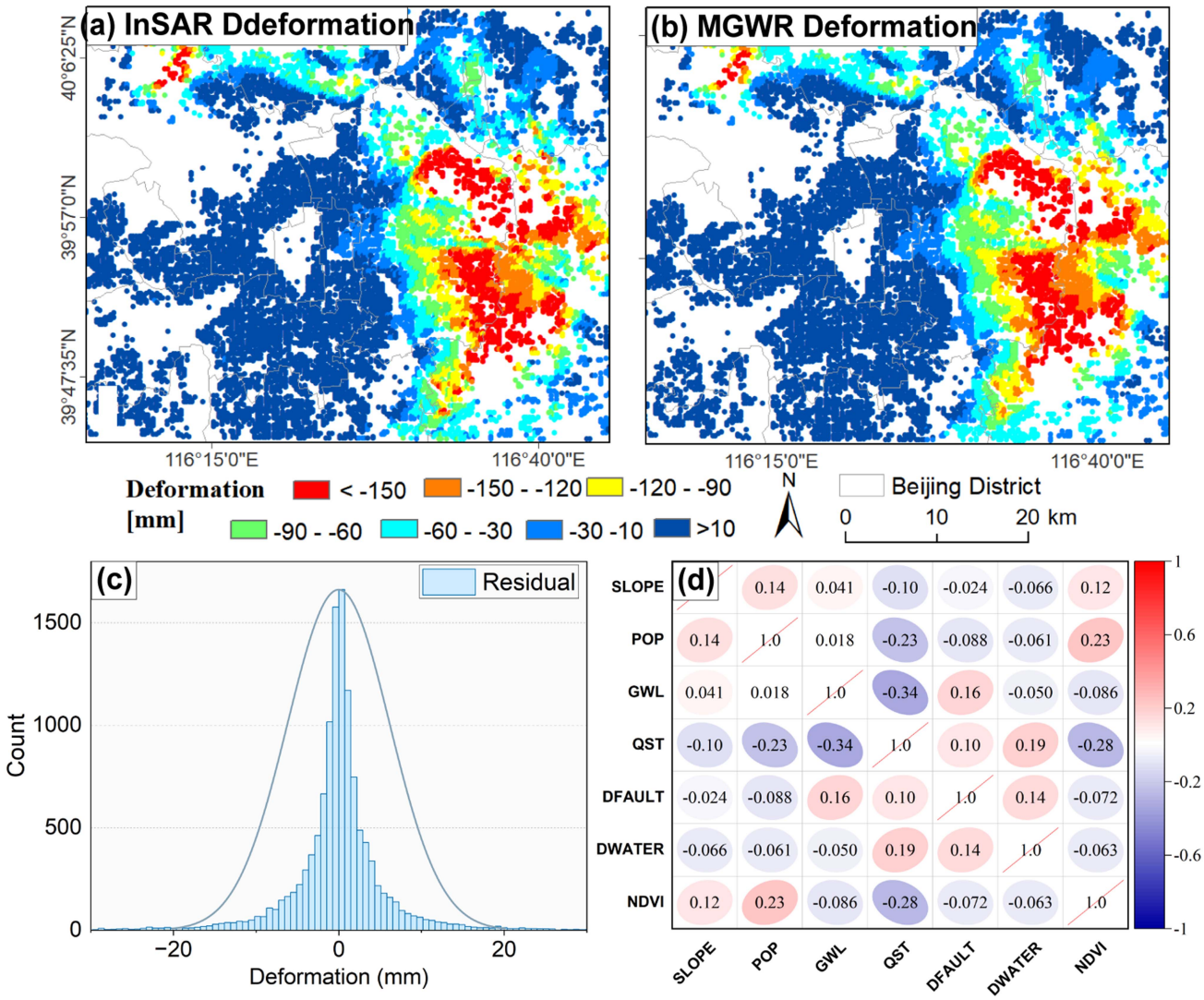

Fig. 8. Results of the MGWR modeling. (a) InSAR deformation. (b) MGWR deformation. (c) Histogram of residuals. (d) Pearson correlations of independent variable.

negative. For compressible layers between 100–150 m, the relationship remains unclear, but a potential positive correlation is suggested [see Fig. 9(b)]. This is consistent with the positive correlation observed in the S3 funnel region and the average correlation coefficient for this region is 1.16 [20].

In the S3 subsidence funnel, the GWL coefficient predominantly exhibits a positive correlation with deformation [see Fig. 9(c)]. The decline in aquifer water levels creates a hydraulic gradient between the clay layer's hydraulic head and the aquifer, driving continuous water release. This process reduces pore pressure and increases the effective stress of the soil layers, leading to ground compaction and indicating that subsidence in this area is still gradually occurring [40]. In contrast, in the S4 subsidence funnel, due to the advancement of the South-to-North Water Transfer and Groundwater Regulation, the GWL in the Beijing Plain has increased. The recovery of aquifer pore pressure has caused an elastic rebound in the aquifer system, leading to a change in the pattern of ground surface deformation in the Chaobai Plain region from subsidence to uplift [12]. Within this region, the coefficients are primarily concentrated between -0.3 and 0.05, with the maximum negative correlation reaching -0.53.

To better investigate the temporal correlation between groundwater and surface deformation, we selected six wells covering two observation periods: April 2022–November 2023, and January 2018–December 2022 [see Fig. 9(c)]. The groundwater was compared with InSAR deformation within a 100 m buffer (see Fig. 10). While the GWL show a consistent rising trend, yet surface deformation responses demonstrate marked spatial heterogeneity. Specifically, at well #38 in the Chaobai Plain, GWL fluctuated by 15 m, deformation progression shifted through two distinct phases.

1) From 2016 to 2018, the subsidence decelerating from −15 mm/yr to stabilization.
2) From 2021 to 2023, an uplift occurred with rate of 10 mm/yr.

This suggests the aquifer recovery toward a new hydraulic equilibrium, forming a new consolidation head [40]. Similar

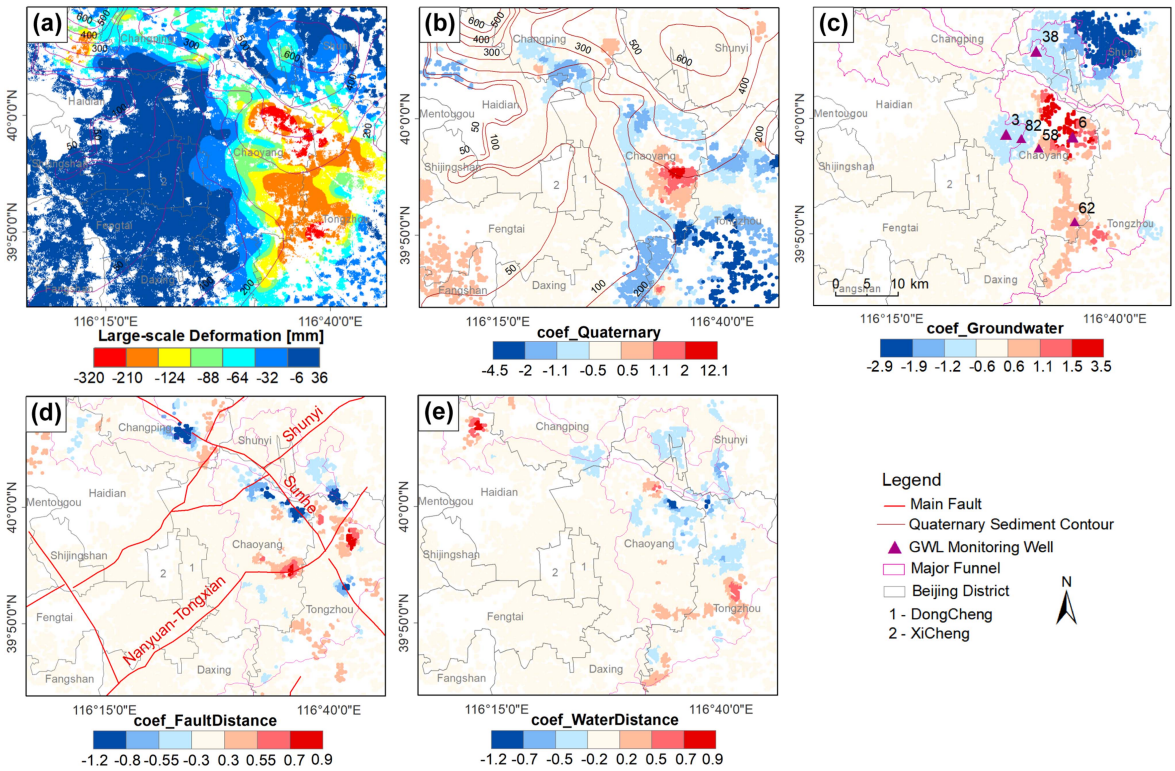

Fig. 9. Large-scale deformation component and the coefficients of influencing factors. (a) Large-scale deformation. (b) Coefficient of Quaternary sediment thickness. (c) Coefficient of groundwater level changes. (d) Coefficient of distance to fault. (e) Coefficient of distance to water system.

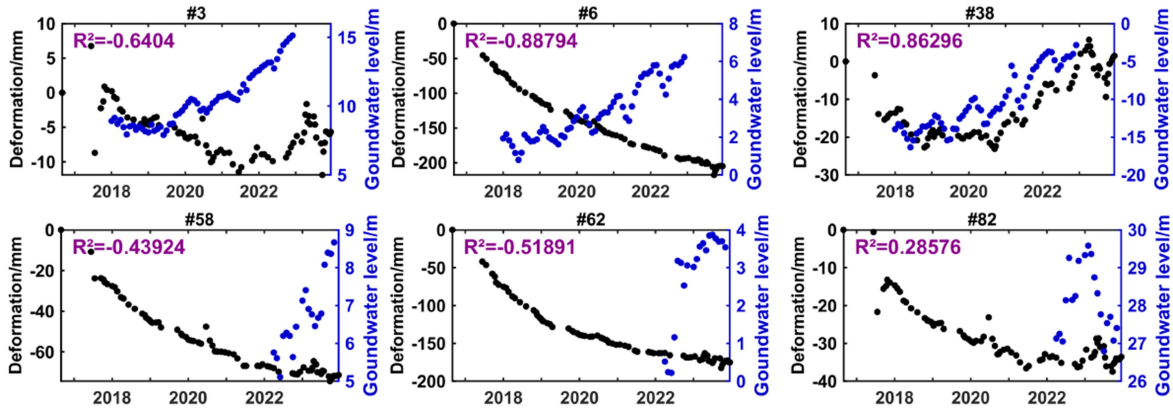

Fig. 10. Comparative time series of surface deformation and groundwater level variations at selected monitoring wells, with well locations labeled in Fig. 9(c).

trends were also been observed at wells #3 and #82, located in Chaoyang District. In contrast, persistent but decelerating subsidence dominate near other well sites. For example, well #6 exhibits seasonal fluctuations in GWL with an overall upward trend at 1 m/yr. However, the deformation still follows a nearly linear subsidence pattern, with a subsidence rate of −25 mm/yr. This may be related to the local hydrogeological constraints, which limits the recharge of groundwater into the aquifer, coupled with the prolonged compaction of deep strata, resulting in a limited deformation response to GWL variations [41].

The effect of DFault on deformation shows notable spatial heterogeneity [see Fig. 9(d)]. the Sunhe Fault exhibits a negative correlation with nearby surface deformation, suggesting that areas near this fault may experience subsidence due to fault activity or the alignment with the direction of water systems. Conversely, the Huangzhuang Fault and the Nanyuan–Tongzhou Fault show positive correlations with surrounding deformation. This is likely due to fault activity inducing stress concentration, causing surface uplift, or partially obstructing groundwater flow, leading to different deformation patterns [40], [42].

The influence of DWater is predominantly negative in areas with dense construction and roads [see Fig. 9(e)]. This is possibly due to impeded water flow, which weakens groundwater recharge effects. Conversely, in areas with more vegetation coverage, such as the center of the S1 subsidence funnel. The abundance of water sources helps stabilize GWL, leading to significant positive influence.

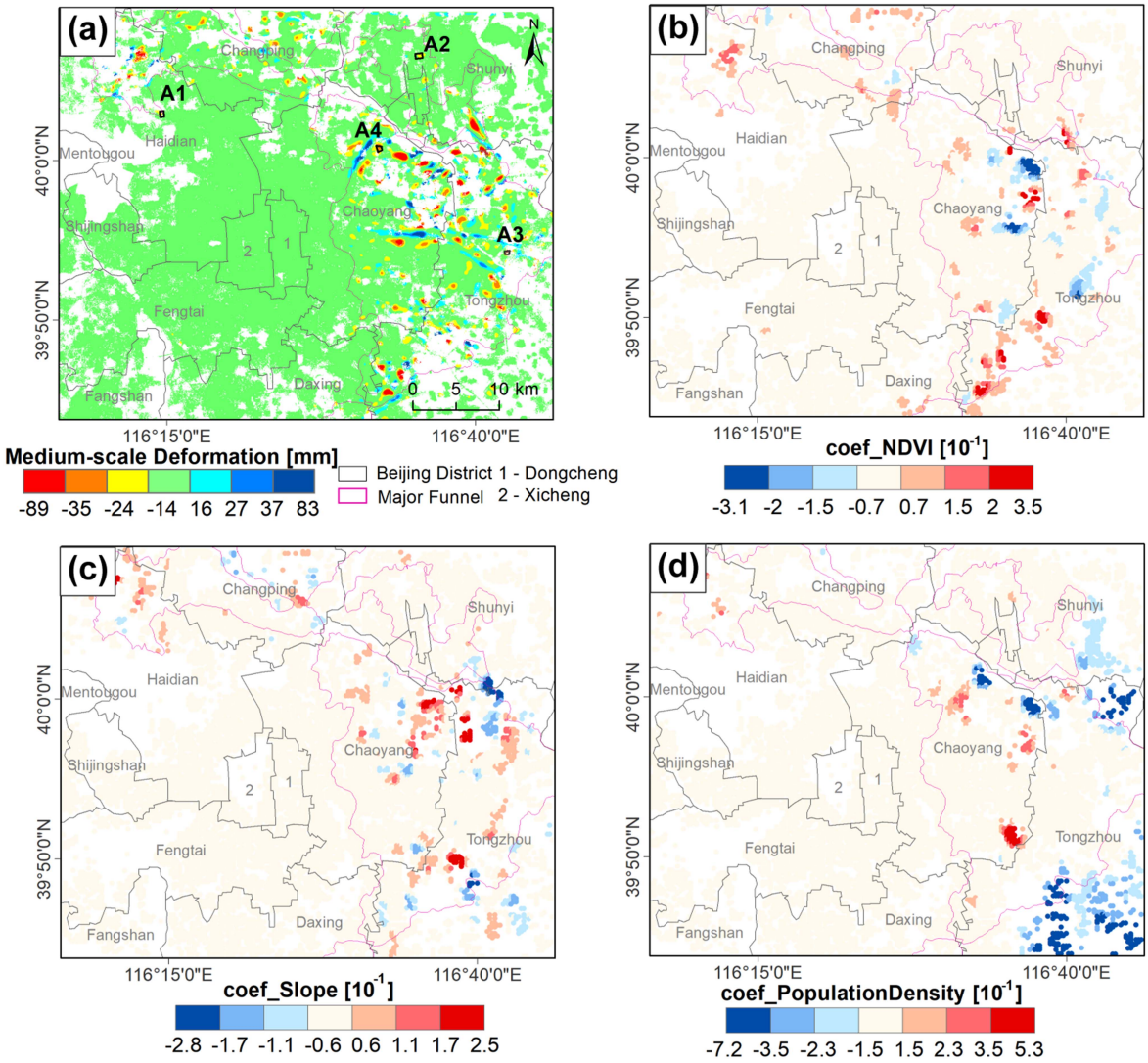

Fig. 11. Medium-scale deformation and influencing factor coefficients. (a) Medium-scale deformation. (b) Coefficient of NDVI. (c) Coefficient of population density. (d) Coefficient of slope.

B. Medium-Scale Deformation

Different from the large-scale deformation, the medium-scale deformation component is closely related to farmland subsidence, soil consolidation, and engineering activities like urban construction, expansion, and renovation [25], [37], [43]. These activities typically cause localized surface deformation in the distance of 1–3 km. Statistics show a significant positive correlation between the frequency of engineering activities in urban areas and the number of deformation monitoring points, indicating that surface subsidence caused by foundation pit dewatering and subsequent building loads during construction has become an important feature of local urban deformation[38], [24], [43].

Although NDVI and population density do not significantly contribute to overall ground deformation [44], spatial analysis reveals a certain degree of correlation between the medium-scale deformation component and both factors. In regions with dense vegetation, such as Changping District, the northwest of Haidian District and areas near rivers, NDVI shows a positive correlation with subsidence signals (see Fig. 11). In particular, the correlation coefficient between deformation and NDVI in the localized subsidence areas of southwest Tongzhou can reach 0.34. This may be related to the regulatory role of vegetation roots on surface water, as areas with higher vegetation cover have root systems that enhance soil stability and reduce the occurrence of surface subsidence. Additionally, vegetation adjusts surface water through transpiration and water cycle regulation, which may help maintain GWL stability and mitigate subsidence caused by groundwater extraction. In contrast, in rapidly urbanizing areas such as central and eastern Chaoyang, the correlation turns negative, with correlation coefficients reaching below -0.2.

Population density shows a predominantly negative correlation with surface deformation in Tongzhou and the peripheral areas of Chaoyang [see Fig. 11(d)]. This indicates that increasing population density may significantly aggregate surface subsidence. Higher population density increases groundwater demand, resulting in excessive groundwater extraction.

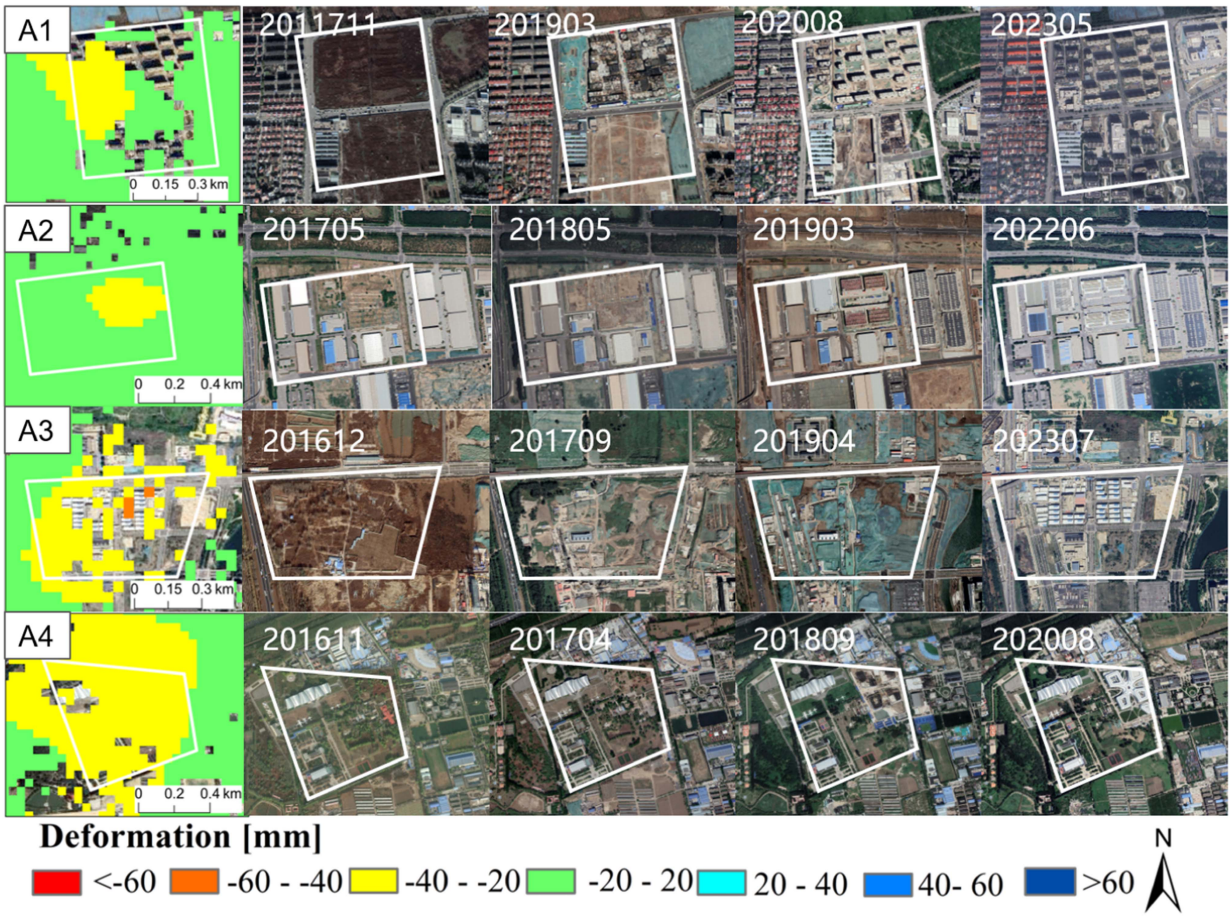

Fig. 12. Historical construction activities in the medium-scale deformation area comparing with optical time elapse images from 2011–2020 (Google Earth).

Thereby, the subsequent decline in the water table promotes subsurface compaction. Urbanization in densely populated areas typically increases building density and additional surface loads, further compressing soil structures and accelerating the subsidence process [38]. However, in some areas of Chaoyang District, particularly the southeastern region, a positive correlation was observed [see Fig. 11(d)]. The average correlation coefficient of around 0.37 and a peak value exceeding 0.5. This phenomenon maybe attributed to other dominant factors, such as groundwater recharge, geological variations, or the regulatory role of vegetation coverage. Moreover, we can find that the slope coefficient exhibits significant spatial variation. Although slope may indirectly influence surface deformation through processes such as surface runoff and soil erosion, no significant correlation between slope and the medium-scale deformation component was observed within the scope and scale of this article. This suggests the diversity and variability of its relationship with subsidence [38].

Since the 21st century, urban construction activities in Beijing have significantly increased, causing noticeable load changes on the surface and leading to localized uneven subsidence [37]. Several typical medium-scale deformation areas related to construction activities were detected, labeled A1 to A4 [see Fig. 11(a)]. These areas reveal surface changes caused by construction activities in different regions, with deformation scales ranging from hundreds of meters to kilometers (see Fig. 12). Among these, A1 and A2 primarily reflect surface changes caused by the construction of medium-scale and small-scale building complexes. The subsidence signals concentrated in the construction areas and rapidly accumulating during the construction period, indicating the direct impact of building loads on local foundations. In contrast, A3 and A4 are located within the S3 subsidence funnel. Here, construction areas are more dispersed, leading to a more fragmented spatial distribution of deformation signals. This phenomenon reflects the impact of the spatial heterogeneity of construction activity layouts and geological conditions on deformation. Overall, these signals reveal the localized impact of urban engineering activities on surface subsidence, further demonstrating that changes in local loads are an important driving factor for inducing uneven subsidence.

C. Small-Scale Deformation

The smallest-scale deformation component exhibits a higher spatial frequency compared to other components. These signals are critical for ensuring urban rail transit safety but are often obscured by large- and medium-scale signals in original InSAR vertical deformation.

Deformation along subway lines is influenced by surface land cover types, as well as ground disturbances and cyclic loading

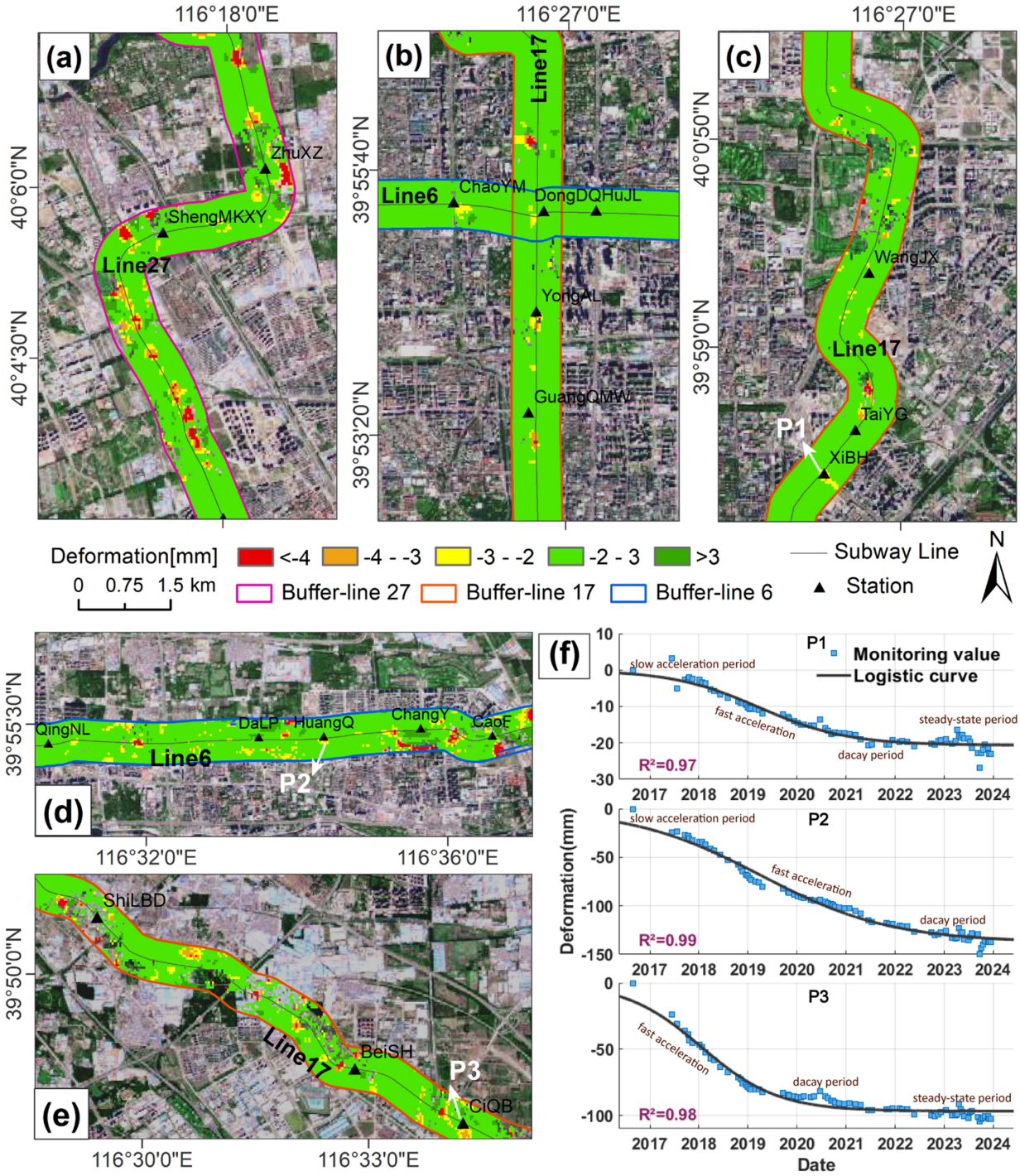

Fig. 13. Small-scale deformation along the subway lines. (a) Local deformation along line 27. (b) Middle segment along line 17. (c) Northern segment along line 17. (d) Local deformation along line 6. (e) Southern segment along line 17. (f) Logistic regression curves of points P1, P2, and P3. The corresponding subway segments are marked in Fig. 7.

caused by train operations during the construction and operational phases [35], [45], [46], [47]. Beijing subway line 27 (also known as the "Changping line") is located in the northwestern part of the Beijing Plain. Its middle section [see Fig. 13(a)] features thick compressible strata, extensive vegetation and bare land, and proximity to highways, which make it susceptible to uneven deformation. Beijing Subway line 17, running in a north-south direction, is divided into three segments based on construction progress. The northern section was opened at the end of 2023 [see Fig. 13(c)], while the middle section [see Fig. 13(b)] remains under construction. Beijing subway line 6, the 15th subway line to open in Beijing, shares its eastern section [see Fig. 13(d)] with the southern section of line 17 [see Fig. 13(c)], both located within the S3 subsidence funnel.

Prolonged operations and geological factors provide potentials for localized deformation.

To validate the correlation between the identified deformation points along subway lines and actual construction or operational activities, three subway stations were selected: Xibahe Station on the northern section of line 17; Ciqubei Station on the southern section of line 17; and Huangqu Station on line 6, denoted as P1, P2, and P3, respectively. The logistic regression effectively illustrates the lifecycle of subway construction, transitioning from a slow acceleration phase to a rapid acceleration phase, followed by deceleration, and ultimately stabilizing [19], [36]. P1, clearly reflects the complete lifecycle of subway construction. After construction began in mid-2017, displacement gradually emerged, accelerating in 2018 and reaching a maximum cumulative deformation of approximately -21 mm by early 2022. Thereafter, the deformation rate slowed and stabilized by the end of 2023 with the line's opening. P2, after construction started in 2018, began to accelerate in deformation. After its opening at the end of 2021, the deformation rate gradually decreased. By 2023, the cumulative deformation had reached approximately -140 mm. Since P3 has been in operation since the end of 2011, its temporal deformation curve does not fully capture the entire deformation lifecycle. However, it also experienced a nearly linear rapid deformation phase in its early stages, gradually stabilizing after 2019 [48]. The results show that the temporal deformation trends at all three stations closely match the Logistic curves.

These above findings demonstrate that the decomposed small-scale deformation can effectively identify subway-related deformation. Similar uneven ground deformation along subway lines may pose significant risks to subway system as shown in Mexico City [23] and Shanghai [24]. Specifically, deformation monitoring at the Olivos metro accident site in Mexico City revealed a subsidence rate gradient of 0.37×10^{-3} year^{-1}, leading to long-term angular distortion and a slope change of up to 3.5%. The resulting differential displacement between columns suggests that angular distortion might have been a contributing factor to structural failure. This also underscores the feasibility of using this approach in separating deformation signals, and facilitating early anomaly detection to mitigate infrastructure risks.

VI. Conclusion

This article proposed a new method for decomposing and analyzing InSAR deformation by the integration of 2D-FFT with the MGWR model. The approach has been successfully applied to the Beijing Plain, utilizing Sentinel-1 data from 2016 to 2023. The main findings regarding multiscale deformation are as follows:

1) Large-scale deformation is mainly associated with subsidence funnels, exhibiting a deformation scale of about 4–8 km, with magnitudes similar to the initial InSAR deformation results. The thickness of Quaternary sediments and fluctuations in GWL influence the extent and severity of large-scale subsidence.
2) The medium-scale deformation component reveals localized subsidence within a range of 1–3 km, primarily located at the centers and peripheries of subsidence funnels, largely driven by urban development activities.
3) The small-scale deformation component displays a lower amplitude of deformation and a less pronounced spatial distribution of < 1 km. It has a strong correlation with the subway as evidenced by decomposed deformation and a logistic regression model.

The proposed method and findings provide valuable insights for understanding urban surface deformation and managing infrastructure safety, both in Beijing and other urban areas. However, the accuracy of deformation separation remains dependent on the thresholds of band-pass filtering in 2D-FFT. Systematic optimization by fusion the geological information and in-situ observation can enhance the reliability of deformation decomposition. Furthermore, integrating higher resolution SAR imagery with deep learning methods offers promising potential to refine deformation separation and probabilistic forecasting of urban infrastructure vulnerability.

Acknowledgment

The Quaternary sediment thickness map and GWL data is from Beijing Survey and Design Institute Company Ltd.

References

[1] J. Du et al., "InSAR-based active landslide detection and characterization along the upper reaches of the Yellow River," *IEEE J. Sel. Topics Appl. Earth Observ. Remote Sens.*, vol. 16, pp. 3819–3830, 2023, doi: 10.1109/JSTARS.2023.3263003.

[2] G. Shi, B. Huang, A. K. Leung, C. W. W. Ng, Z. Wu, and H. Lin, "Millimeter slope ratcheting from multitemporal SAR interferometry with a correction of coastal tropospheric delay: A case study in Hong Kong," *Remote Sens. Environ.*, vol. 280, Oct. 2022, Art. no. 113148, doi: 10.1016/j.rse.2022.113148.

[3] X. Wenbin, L. Xingjun, Z. Jianjun, W. Jiageng, and X. Lei, "Review of volcano deformation monitoring and modeling with InSAR," *Geomatics Inf. Sci. Wuhan Univ.*, vol. 48, no. 10, pp. 1632–1642, 2023, doi: 10.13203/j.whugis20230090.

[4] N. Fang et al., "An enhanced spectral diversity coregistration method for dual-polarimetric Sentinel-1A/B TOPS data," *Geodesy Geodyn.*, vol. 14, no. 5, pp. 431–437, Sep. 2023, doi: 10.1016/j.geog.2023.02.003.

[5] H. Liu, L. Xie, G. Zhao, E. Ali, and W. Xu, "A joint InSAR-GNSS workflow for correction and selection of interferograms to estimate high-resolution interseismic deformations," *Satell. Navig.*, vol. 4, no. 1, Dec. 2023, Art. no. 14, doi: 10.1186/s43020-023-00105-6.

[6] Y. Liu, C. Zhao, Q. Zhang, C. Yang, and J. Zhang, "Land subsidence in Taiyuan, China, monitored by InSAR technique with multi sensor SAR datasets from 1992 to 2015," *IEEE J. Sel. Topics Appl. Earth Observ. Remote Sens.*, vol. 11, no. 5, pp. 1509–1519, May 2018, doi: 10.1109/JSTARS.2018.2802702.

[7] Y. Liu et al., "Removal of atmospheric effects on ground based radar interferometry by using ICA: A case study in Shenzhen, China," in *Proc. IGARSS IEEE Int. Geosci. Remote Sens. Symp.*, 2023, pp. 8246–8248, doi: 10.1109/IGARSS52108.2023.10281751.

[8] P. Ma et al., "Remotely sensing large- and small-scale ground subsidence: A case study of the Guangdong–Hong Kong–Macao Greater Bay Area of China," *Remote Sens. Environ.*, vol. 232, Oct. 2019, Art. no. 111282, doi: 10.1016/j.rse.2019.111282.

[9] Z. Jianjun, L. Zhiwei, and J. Hu, "Research progress and methods of InSAR for deformation monitoring," *Acta Geodaetica et Cartographica Sinica*, vol. 46, no. 10, pp. 1717–1733, 2017, doi: 10.11947/j.AGCS.2017.20170350.

[10] H. Yang et al., "Identification and analysis of deformation areas in the construction stage of pumped storage power station using GB-InSAR technology," *IEEE J. Sel. Topics Appl. Earth Observ. Remote Sens.*, vol. 16, pp. 4931–4946, 2023, doi: 10.1109/JSTARS.2023.3281824.
[11] F. Cigna and D. Tapete, "Present-day land subsidence rates, surface faulting hazard and risk in Mexico City with 2014–2020 Sentinel-1 IW InSAR," *Remote Sens. Environ.*, vol. 253, Feb. 2021, Art. no. 112161, doi: 10.1016/j.rse.2020.112161.
[12] J. Dong et al., "Tri-decadal evolution of land subsidence in the Beijing Plain revealed bymulti-epoch satellite InSAR observations," *Remote Sens. Environ.*, vol. 286, Mar. 2023, Art. no. 113446, doi: 10.1016/j.rse.2022.113446.
[13] Y. Zheng et al., "Spatial and temporal evolution of ground subsidence in the Beijing plain area using long time series interferometry," *IEEE J. Sel. Topics Appl. Earth Observ. Remote Sens.*, vol. 16, pp. 153–165, 2023, doi: 10.1109/JSTARS.2022.3223027.
[14] Z. Zhang et al., "Monitoring and analysis of ground subsidence in Shanghai based on PS-InSAR and SBAS-InSAR technologies," *Sci. Rep.*, vol. 13, no. 1, May 2023, Art. no. 8031, doi: 10.1038/s41598-023-35152-1.
[15] S. Ahmed, Y. Hiraga, and S. Kazama, "Land subsidence in Bangkok vicinity: Causes and long-term trend analysis using InSAR and machine learning," *Sci. Total Environ.*, vol. 946, Oct. 2024, Art. no. 174285, doi: 10.1016/j.scitotenv.2024.174285.
[16] B. Chen et al., "Characterization and causes of land subsidence in Beijing, China," *Int. J. Remote Sens.*, vol. 38, no. 3, pp. 808–826, Feb. 2017, doi: 10.1080/01431161.2016.1259674.
[17] C. Zhou et al., "Reduced rate of land subsidence since 2016 in Beijing, China: Evidence from Tomo-PSInSAR using RadarSAT-2 and Sentinel-1 datasets," *Int. J. Remote Sens.*, vol. 41, no. 4, pp. 1259–1285, Feb. 2020, doi: 10.1080/01431161.2019.1662967.
[18] W. Chen, H. Gong, B. Chen, K. Liu, M. Gao, and C. Zhou, "Spatiotemporal evolution of land subsidence around a subway using InSAR time-series and the entropy method," *GISci. Remote Sens.*, vol. 54, no. 1, pp. 78–94, Jan. 2017, doi: 10.1080/15481603.2016.1257297.
[19] L. Duan et al., "An improved multi-sensor MTI time-series fusion method to monitor the subsidence of Beijing Subway network during the past 15 years," *Remote Sens.*, vol. 12, no. 13, Jul. 2020, Art. no. 2125, doi: 10.3390/rs12132125.
[20] S. Lai, J. Lin, J. Dong, J. Wu, X. Huang, and M. Liao, "Investigating overlapping deformation patterns of the Beijing Plain by independent component analysis of InSAR observations," *Int. J. Appl. Earth Observ. Geoinf.*, vol. 135, Dec. 2024, Art. no. 104279, doi: 10.1016/j.jag.2024.104279.
[21] H. Xu et al., "Spatio-temporal analysis of land subsidence in Beijing plain based on InSAR and PCA," *Spectrosc. Spectral Anal.*, vol. 42, no. 7, pp. 2315–2324, 2022, doi: 10.3964/j.issn.1000-0593(2022)07-2315-10.
[22] D. Solano-Rojas, S. Wdowinski, E. Cabral-Cano, and B. Osmanoğlu, "Detecting differential ground displacements of civil structures in fast-subsiding metropolises with interferometric SAR and band-pass filtering," *Sci. Rep.*, vol. 10, no. 1, Sep. 2020, Art. no. 15460, doi: 10.1038/s41598-020-72293-z.
[23] D. Solano-Rojas, S. Wdowinski, E. Cabral-Cano, and B. Osmanoğlu, "Geohazard assessment of Mexico City's Metro system derived from SAR interferometry observations," *Sci. Rep.*, vol. 14, no. 1, Mar. 2024, Art. no. 6035, doi: 10.1038/s41598-024-53525-y.
[24] R. Wang, M. Yang, T. Yang, J. Lin, and M. Liao, "Decomposing and mapping different scales of land subsidence over Shanghai with X- and C-band SAR data stacks," *Int. J. Digit. Earth*, vol. 15, no. 1, pp. 478–502, Dec. 2022, doi: 10.1080/17538947.2022.2036835.
[25] Z. Wu, P. Ma, Y. Zheng, F. Gu, L. Liu, and H. Lin, "Automatic detection and classification of land subsidence in deltaic metropolitan areas using distributed scatterer InSAR and Oriented R-CNN," *Remote Sens. Environ.*, vol. 290, May 2023, Art. no. 113545, doi: 10.1016/j.rse.2023.113545.
[26] P. Berardino, G. Fornaro, R. Lanari, and E. Sansosti, "A new algorithm for surface deformation monitoring based on small baseline differential SAR interferograms," *IEEE Trans. Geosci. Remote Sens.*, vol. 40, no. 11, pp. 2375–2383, Nov. 2002.
[27] U. Wegmüller and C. Werner, "Gamma SAR processor and interferometry software," 1997.
[28] Y. Chen, C. Xu, Y. Ge, X. Zhang, and Y. Zhou, "A 100 m gridded population dataset of China's seventh census using ensemble learning and big geospatial data," *Earth Syst. Sci. Data*, vol. 16, no. 8, pp. 3705–3718, Aug. 2024, doi: 10.5194/essd-16-3705-2024.
[29] S. Jiao et al., "Multi-scale analysis of surface building density and land subsidence using a combination of wavelet transform and spatial autocorrelation in the plains of Beijing," *Sustainability*, vol. 16, no. 7, Mar. 2024, Art. no. 2801, doi: 10.3390/su16072801.
[30] E. Keogh et al., "Segmenting time series: A survey and novel approach," *Data Mining Time Ser. Databases*, vol. 57, pp. 1–22, 2004.
[31] R. C. Gonzalez, *Digital Image Processing*. New York, NY, USA: Pearson Educ., 2018.
[32] C. Brunsdon, A. S. Fotheringham, and M. E. Charlton, "Geographically weighted regression: A method for exploring spatial nonstationarity," *Geographical Anal.*, vol. 28, no. 4, pp. 281–298, Oct. 1996, doi: 10.1111/j.1538-4632.1996.tb00936.x.
[33] T. Oshan, Z. Li, W. Kang, L. Wolf, and A. Fotheringham, "MGWR: A Python implementation of multiscale geographically weighted regression for investigating process spatial heterogeneity and scale," *ISPRS Int. J. Geo-Inf.*, vol. 8, no. 6, Jun. 2019, doi: 10.3390/ijgi8060269.
[34] Z. Xiuxing et al., "The subsidence monitoring along Beijing Subway network based on MT-InSAR," *J. Geo-Inf. Sci.*, vol. 20, no. 12, pp. 1810–1819, 2018, doi: 10.12082/dqxxkx.2018.180322.
[35] B. Hu and Z. Li, "Time-series InSAR technology for ascending and descending orbital images to monitor surface deformation of the Metro network in Chengdu," *IEEE J. Sel. Topics Appl. Earth Observ. Remote Sens.*, vol. 14, pp. 12583–12597, 2021, doi: 10.1109/JSTARS.2021.3130584.
[36] H. Wang et al., "Deriving spatio-temporal development of ground subsidence due to subway construction and operation in delta regions with PS-InSAR data: A case study in Guangzhou, China," *Remote Sens.*, vol. 9, no. 10, Sep. 2017, Art. no. 1004, doi: 10.3390/rs9101004.
[37] Q. Yang et al., "Multi-scale analysis of the relationship between land subsidence and buildings: A case study in an eastern Beijing urban area using the PS-InSAR technique," *Remote Sens.*, vol. 10, no. 7, Jun. 2018, Art. no. 1006, doi: 10.3390/rs10071006.
[38] Z. Wu, X. Zhang, J. Cai, M.-P. Kwan, H. Lin, and P. Ma, "Understanding spatially nonstationary effects of natural and human-induced factors on land subsidence based on multi-temporal InSAR and multi-source geospatial data: A case study in the Guangdong-Hong Kong-Macao Greater Bay Area," *Int. J. Digit. Earth*, vol. 16, no. 2, pp. 4404–4427, Dec. 2023, doi: 10.1080/17538947.2023.2271882.
[39] L. Kunchao et al., "Distribution characteristics and influencing factors of land subsidence in Beijing plain," *Geol. China*, vol. 43, no. 6, pp. 2216–2225, 2016.
[40] D. Meng et al., "Land subsidence and rebound response to groundwater recovery in the Beijing plain: A new hydrological perspective," *J. Hydrol. Reg. Stud.*, vol. 57, Feb. 2025, Art. no. 102127, doi: 10.1016/j.ejrh.2024.102127.
[41] S. Lai, J. Lin, J. Dong, J. Wu, X. Huang, and M. Liao, "Investigating overlapping deformation patterns of the Beijing plain by independent component analysis of InSAR observations," *Int. J. Appl. Earth Observ. Geoinf.*, vol. 135, Dec. 2024, Art. no. 104279, doi: 10.1016/j.jag.2024.104279.
[42] L. Hu et al., "Land subsidence in Beijing and its relationship with geological faults revealed by Sentinel-1 InSAR observations," *Int. J. Appl. Earth Observ. Geoinf.*, vol. 82, Oct. 2019, Art. no. 101886, doi: 10.1016/j.jag.2019.05.019.
[43] M. Sun, Y. Du, Q. Liu, G. Feng, X. Peng, and C. Liao, "Understanding the spatial-temporal characteristics of land subsidence in Shenzhen under rapid urbanization based on MT-InSAR," *IEEE J. Sel. Topics Appl. Earth Observ. Remote Sens.*, vol. 16, pp. 4153–4166, 2023, doi: 10.1109/JSTARS.2023.3264652.
[44] Q. Ding, Z. Shao, X. Huang, O. Altan, Q. Zhuang, and B. Hu, "Monitoring, analyzing and predicting urban surface subsidence: A case study of Wuhan City, China," *Int. J. Appl. Earth Observ. Geoinf.*, vol. 102, Oct. 2021, Art. no. 102422, doi: 10.1016/j.jag.2021.102422.
[45] S. Wu, B. Zhang, H. Liang, C. Wang, X. Ding, and L. Zhang, "Detecting the deformation anomalies induced by underground construction using multiplatform MT-InSAR: A case study in to Kwa Wan Station, Hong Kong," *IEEE J. Sel. Topics Appl. Earth Observ. Remote Sens.*, vol. 14, pp. 9803–9814, 2021, doi: 10.1109/JSTARS.2021.3113672.
[46] M. Yang, R. Wang, M. Li, and M. Liao, "A PSI targets characterization approach to interpreting surface displacement signals: A case study of the Shanghai metro tunnels," *Remote Sens. Environ.*, vol. 280, Oct. 2022, Art. no. 113150, doi: 10.1016/j.rse.2022.113150.
[47] J. Zhang et al., "Spatiotemporal-grained quantitative assessment of construction-induced deformation along the MTR in Hong Kong using MT-InSAR and iterative STL-based subsidence ratio analysis," *Int. J. Appl. Earth Observ. Geoinf.*, vol. 136, Feb. 2025, Art. no. 104342, doi: 10.1016/j.jag.2024.104342.
[48] Z. Bai, Y. Wang, and T. Balz, "Beijing land subsidence revealed using PS-InSAR with long time series TerraSAR-X SAR data," *Remote Sens.*, vol. 14, no. 11, May 2022, Art. no. 2529, doi: 10.3390/rs14112529.

Nian Feng received the B.Sc. degree in geographic information science from China University of Mining and Technology, Xuzhou, China, in 2022. She is currently working toward the master's degree in photogrammetry and remote sensing with Central South University, Changsha, China.

Her research interests include InSAR, ground subsidence, and infrastructure deformation monitoring.

Lei Xie received the bachelor's degree in surveying and mapping engineering from China University of Geosciences, Wuhan, China, in 2014, the master's degree in geomatics engineering from the University of Calgary, Calgary, AB, Canada, in 2018, and the Ph.D. degree in geodesy from the Hong Kong Polytechnic University, Hong Kong, in 2022.

He is currently a Lecturer with the School of Geosciences and Info-Physics, Central South University, Changsha, China. His research interests include InSAR, geodynamics, and applications in infrastructure monitoring.

Wenbin Xu received the Ph.D. degree in geophysics from King Abdullah University of Science and Technology, Thuwal, Saudi Arabia, in 2015.

He was a Postdoc Researcher with the Berkeley Earthquake Laboratory, University of California, Berkeley and an Assistant Professor with the Department of Land Surveying and Geo-Informatics, the Hong Kong Polytechnic University, Kowloon, Hong Kong. He is currently a Professor and leads the Lab of Volcano and Earthquake Research with the School of Geoscience and Info-Physics, Central South University, Changsha, China. His research primarily focuses on the use of space geodesy to study ground deformation associated with a variety of geophysical and anthropogenic processes.

Miao Yu received the Ph.D. degree in geographic information science from China University of Geosciences, Beijing, China, in 2003.

In 2013, she was with the postdoctoral workstation of the Institute of Remote Sensing of the Chinese Academy of Sciences to conduct scientific research. In 2016, she was with Beijing Urban Construction Survey, Design and Research Institute Company Ltd., Beijing, China. Her work and research contents include the research and application of geographic information system, the technical application of artificial intelligence in rail transit, and the application of synthetic aperture radar interferometry (InSAR) in the monitoring of rail transit infrastructure.